

Scattered neutron background in thermal neutron detectors

E. Dian^{a,b,c,*}, K. Kanaki^b, G. Ehlers^d, R.J. Hall-Wilton^{b,e}, A. Khaplanov^b,
T. Kittelmann^b, P. Zagyvai^{a,c}

^a*Hungarian Academy of Sciences, Centre for Energy Research, 1525 Budapest 114., P.O. Box 49., Hungary*

^b*European Spallation Source ESS ERIC, P.O Box 176, SE-221 00 Lund, Sweden*

^c*Budapest University of Technology and Economics, Institute of Nuclear Techniques, 1111 Budapest, Műegyetem rakpart 9., Hungary*

^d*Oak Ridge National Lab, Neutron Technologies Division, Oak Ridge, TN 37831-6475, USA*

^e*Mid-Sweden University, SE-851 70 Sundsvall, Sweden*

Abstract

Inelastic neutron scattering instruments require very low background; therefore the proper shielding for suppressing the scattered neutron background, both from elastic and inelastic scattering is essential. The detailed understanding of the background scattering sources is required for effective suppression. The Multi-Grid thermal neutron detector is an Ar/CO₂ gas filled detector with a ¹⁰B₄C neutron converter coated on aluminium substrates. It is a large-area detector design that will equip inelastic neutron spectrometers at the European Spallation Source (ESS). To this end a parameterised Geant4 model is built for the Multi-Grid detector. This is the first time thermal neutron scattering background sources have been modelled in a detailed simulation of detector response. The model is validated via comparison with measured data of prototypes installed on the IN6 instrument at ILL and on the CNCS instrument at SNS. The effect of scattering originating in detector components is smaller than effects originating elsewhere.

Keywords: ESS, neutron detector, neutron scattering, Monte Carlo simulation, Geant4, validation

*Corresponding author

Email address: dian.eszter@energia.mta.hu (E. Dian)

1. Introduction

Inelastic neutron scattering is a very powerful technique for exploring atomic and molecular motion, as well as magnetic and crystal field excitations [1]. Time-of-Flight (ToF) spectrometers allow a broad phase space to be measured in a single setting; this is typically achieved with a large area detector array [2]. In typical state-of-the-art neutron instruments [2–8], this detector array can be 10–50 m². One of the main performance criteria of these spectrometers is typically defined by the Signal-to-Background Ratio (SBR), therefore understanding and enhancing the latter is important for the instrument optimisation. In particular, scattered neutrons have a significant contribution to the SBR. The estimation of the SBR is done currently on a series of prescriptions based on observations of historical instrument installation.

As a consequence of the recent restructuring of the ³He market [9], a need for cost effective ³He-replacing detector solutions is raised [10], especially for inelastic neutron scattering instruments, where large area detectors with high SBR are required. A potent new solution for this type of instruments is the Multi-Grid detector [11; 12], which will be used for the three Time-of-Flight chopper spectrometers at ESS [13–16]. The Multi-Grid design was invented at the Institut Laue-Langevin (ILL) [17; 18], and the detector now is jointly developed by the ILL and the ESS within the CRISP [19] and BrightnESS [20] projects.

The Multi-Grid detector is an Ar/CO₂-filled proportional chamber with a solid boron-carbide (¹⁰B₄C) neutron converter, enriched in ¹⁰B [21–23]. The basic unit of the Multi-Grid detector is the grid, an aluminium frame; thin aluminium lamellas, coated on their both sides with boron-carbide, the so called blades are placed in this frame, parallel with each other and the entrance window of the grid, dividing the grid into cells. In the detector the grids are structured into columns, and this way the cells one above the other form tubes, and the signals are readout both from the frames and the anode wires that go through

the whole length of the column in the centre of the cells. The planned detector modules and the prototypes are built of these columns. A series of small size prototypes and large scale demonstrators are already built and tested at different sources and instruments [24; 25], and the development of the detector has already entered the up-scaling phase. As Multi-Grid is a large area detector, full scale design is limited by cost considerations. However, detailed Monte Carlo modelling can help tackle the limitations and provide guidelines for the up-scaling design, which is particularly important for detectors that have to provide excellent SBR $\sim \mathcal{O}(10^5)$.

The two-fold aim of the current study is to introduce a detailed Geant4 model of the Multi-Grid detector including validation against datasets of experiments [24; 25] performed on existing demonstrators, as well as to identify the various components of the scattered neutron background, induced by cold and thermal neutrons internally and externally to the Multi-Grid detector.

The Geant4 model of the Multi-Grid detector is presented in Section 2. In Section 3, the model validation against the measured ToF flight distance and energy transfer data from the IN6 (Cold neutron time-focusing time-of-flight spectrometer IN6-Sharp), and in Sections 4.1 and 4.2 the CNCS (Cold Neutron Chopper Spectrometer) demonstrator tests are shown. As part of the reproduction of the CNCS demonstrator measured data, a study of the individual contributions to the scattered neutron background is also discussed. In Section 4.3 results regarding the neutron scattering on the aluminium components of the detector vessel of the CNCS detector are described. Finally, in Section 5 the obtained results are concluded from the aspects of validation, and the further utilisation of the built model for detailed background analysis and for the optimisation of the detector vessel design is also shown.

2. Geant4 model of Multi-Grid detector

A general, parameterised Geant4 [26–28] model of the Multi-Grid detector has been developed within the ESS Detector Group Simulation Framework [29],

with the usage of the NXSG4 [30] extension library. The latter enables the crystalline structure of aluminium, used in the detector frame. For all other components, standard Geant4 materials are used. The physics list is the standard QGSP_BIC_HP, except when polyethylene is included in the materials, in which case a customised physics list is preferred instead [31], due to the relevance of thermal scattering on the high hydrogen-content of the polyethylene.

From the flexible, full-scale model, the realistic models of two demonstrators that were tested at the IN6 [24] at ILL and at the CNCS [25] at SNS were also prepared. To reach a very flexible geometry, a few simplifications were done.

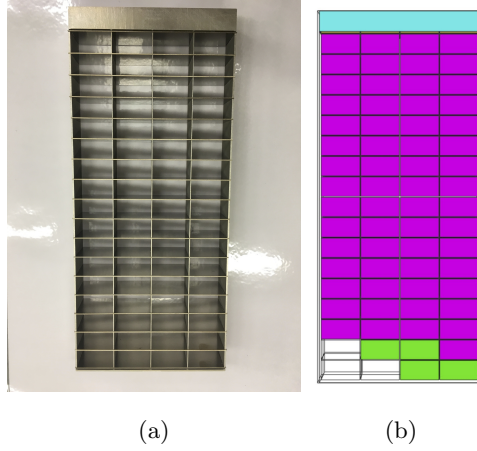


Figure 1: Real grid (1a) and grid geometry implemented in Geant4 (1b).

The basic unit of the model is the so called cell, a $2 \times 2 \times 1 \text{ cm}^3$ counting gas volume of the detector, delimited by B_4C -coated aluminium blades. Therefore everything has to be symmetrical at the cell level, like the blade thicknesses, the cell volumes and most importantly the coating thicknesses. This estimation is applied in the basic model and the IN6, but in the CNCS demonstrator a series of different coating thicknesses are used ($13 \times 0.5 \mu\text{m} + 14 \times 1.0 \mu\text{m} + 6 \times 1.5 \mu\text{m} + 1 \times 1.0 \mu\text{m}$). So for the latter model, the coating thicknesses are hard-coded to fit the real prototype, and so the grid became the basic unit for this detector. The anode wires and the electronics of the detector are excluded from the models, as it is shown in Figure 1. The major parameters of the prepared

models are shown in Table 1.

The simulated primary neutrons are generated at the sample position. The sample is placed at the centre of the geometry, with the z direction chosen as the beam direction, leading to x as horizontal and to y as vertical coordinates. The sample-to-detector distance is defined as the shortest distance from the sample position to the entrance window of the detector: grid window or vessel window, in case the latter is enabled. Basic particle guns, like a pencil beam, 4π and cylindrical sources are used, as well as targeted beams to irradiate only the detector surface. Although the physics of the samples themselves is not implemented in the simulations, the above listed particle guns are defined both as point and volume sources ($1 \times 1 \times 1 \text{ cm}^3$ cube or cylinder with 1 cm diameter). Some instrument effects are introduced via the source definition, like the energy distribution of the incident primary neutrons.

In chopper spectroscopy the data of interest are the momentum- and energy transfer of the scattered neutrons. These are derived from the primary measured quantities: the detection coordinates (giving the flight distance) and the ToF. The flight distance is defined as the distance from the sample position to the detection coordinates. The simulated detection coordinates are reduced to the centre of the cell in which the neutron is detected, despite the higher resolution of the simulation. ToF is simulated from sample position. The detector model is validated against these raw measured quantities of the IN6 demonstrator, and a detailed study of scattered neutron background is also performed regarding the energy transfer in the CNCS demonstrator.

3. Model of demonstrator test on the IN6 instrument at ILL

At the IN6 experiment the demonstrator (Figure 2a) is tested with neutron beams of 4.1, 4.6 and 5.1 Å (i.e. 4.87, 3.87 and 3.15 meV, respectively), irradiating the entire entrance surface. The same geometry is implemented in the simulation (Figure 2b) and validated against the measured and published ToF spectra. Due to the lack of data on the measurement setup (e.g., exact chop-

Table 1: Major default geometrical parameters of Multi-Grid detector models.

Parameter		Default value		
		Basic model	IN6 model	CNCS model
Number of cells	width (x)	4	4	4
	depth (z)	17	17	17
Number of grids in columns		127	16	48
Number of columns		125 ¹	6	2
Cell size	width (x)	2.2 cm	2.2 cm	2.2 cm
	height (y)	2.26 cm	2.26 cm	2.25 cm
	depth (z)	1.1 cm	1.1 cm	1.1 cm
Coating thickness		1.0 μm	1.0 μm	0.5-1.5 μm
Entrance window thickness		1.0 mm	1.0 mm	2.0 mm
Frame end thickness		11.6 mm	11.6 mm	12.5 mm
Frame side thickness		1.0 mm	1.0 mm	1.0 mm
Blade thickness	orthogonal (z)	0.6 mm	0.6 mm	0.5 mm
	parallel (x)	0.5 mm	0.5 mm	0.5 mm
End shielding thickness		1.0 mm	10^{-7} mm^2	1 mm
Side shielding thickness		1.0 mm	0 mm	0 mm
Grid gap thickness		1.0 mm	1.0 mm	1.0 mm
Sample-detector front face distance		4 m	2.48 m	3.33 m
Physics list		QGSP_BIC_HP		
Frame material		Al	Al	Al
Counting gas		Ar/CO ₂	Ar/CO ₂	Ar/CO ₂
		80/20	90/10	80/20
Coating		¹⁰ B ₄ C	¹⁰ B ₄ C	¹⁰ B ₄ C
		97 % enriched	97 % enriched	97 % enriched
End shielding		PE+Gd ₂ O ₃	-	PE+Gd ₂ O ₃
Modules		no	no	yes
Vessel		-	-	yes

¹Number of columns defined to build a typical 180° detector arc.

²End shielding is implemented as a volume of PE+Gd₂O₃, therefore 0 mm thickness is not allowed by the code. Lack of shielding was obtained with the minimum applicable thickness.

per settings and timing references), the measured and simulated ToF spectra are compared either in a relative time scale, or all of them are scaled to the time scale of the simulation, in which the neutrons and their respective ToF are generated at the sample position.

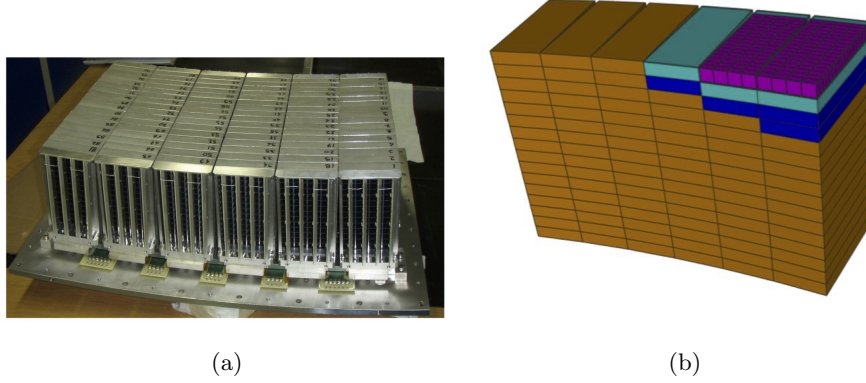


Figure 2: As built IN6 prototype (2a) and its Geant4 model (2b).

The detector geometry is irradiated with pencil and targeted beams, in order to illuminate the entrance surface (see Figure 3), both with sharply mono-energetic and Gauss-smeared initial neutron energy distributions of 4.1, 4.6 and 5.1 Å. For preparing the demonstrative study on the 2-dimensional distributions of the ToF spectra as the function of the depth of detection, a minor simplification was performed: for this demonstration only 1 column of the detector model was used, since in this case z-coordinate one-to-one corresponds to the detection depth in detector, leading to an easy readout.

3.1. Simulation results for IN6 Demonstrator detector

For the IN6 experiment, ToF spectra and 2D detection depth dependent ToF spectra are simulated and compared to the published measurements at 4.1, 4.6 and 5.1 Å wavelengths. In Figure 4 the comparison of the measured (Figures 4a – 4c) and the simulated ToF-spectra as a function of the depth of detection is presented with mono-energetic (Figures 4d – 4f) and Gaussian (Figures 4g – 4i) incident neutron energy distributions. At all wavelengths the main path

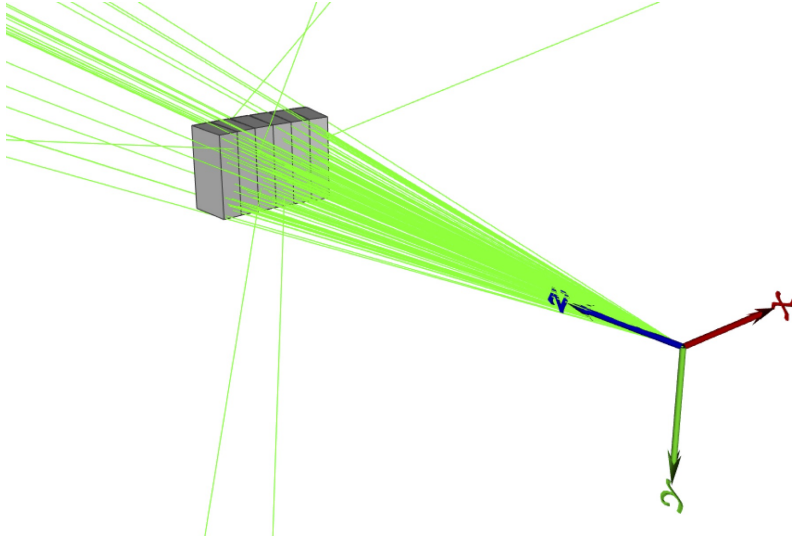


Figure 3: Geometry view of the IN6 Geant4 detector model irradiated with targeted beam.

of the incident detected neutrons clearly appears as a skew line both in the measured and the simulated distributions. The angle of the path is related to the neutron's velocity.

Beside the main path, at 4.1 and 4.6 Å wavelengths that are below the aluminium Bragg edge [32; 33], the traces of the detected scattered neutrons appear as well. On the one hand, in the near surface region a triangle-shaped shadow appears beside the main neutron path, produced by the neutrons detected after scattering on the intermediate aluminium blades. On the other hand, a short, opposite direction skew line appears for these two wavelengths, both in the measured and simulated distributions, starting from the unshielded rear end of the detector, caused by a significant fraction of scattered neutrons coming from the detector end blade. Both effects are caused by the Bragg-scattering on aluminium and emphasise the need for targeted shielding in the detector.

With the reproduction of these ToF characteristics and scattering phenomena, the developed Geant4 model is qualitatively validated. For a quantitative validation, 1D ToF histograms are also simulated.

The simulated ToF spectra are quantitatively compared with the measured

ones for all three wavelengths. The simulations are produced with the same Gaussian initial energy distributions that were previously applied for the 2D ToF-depth studies. The standard deviations of the distributions are estimated to fit both the typical instrument energy resolution and the measured ToF data. In Figure 5 the measured and simulated ToF spectra are presented in a relative time scale. The IN6 Multi-Grid demonstrator has a considerable α -background [34], coming from the uranium and thorium content of the non-purified aluminium of the grids. This background is random and evenly distributed in time. Therefore, updated simulated spectra are reproduced for all wavelengths, where a subsequent background correction is applied. This is performed with a continuous, flat time-constant background added to the simulated ToF spectra, in order to obtain a better comparison with the measured results. The background is estimated to fit the average measured background. In the case of 5.1 Å, the background is not entirely flat, which is presumably caused by additional effects of the measurement setup and the instrument. As an example, adding the resolution [35] of the Fermi-chopper in the model would give a better description of the tails of the Gaussian ToF peaks. Due to lack of additional information it is impossible to estimate these effects.

Figure 5 demonstrates that the measured and simulated ToF peaks agree at all the studied wavelengths. Moreover, by applying a correction of a continuous background, the right-hand-side decrease of the ToF spectrum is also reproduced quantitatively, with only a small discrepancy in the values at 4.1 and 4.6 Å.

These analysis results of the IN6 model and data serve as quantitative validation of the Multi-Grid simulation.

The now validated model is applicable to general Multi-Grid irradiation setups, like the CNCS demonstrator test, for identifying detector and instrument background effects.

4. Model of demonstrator test on CNCS instrument at SNS

A two-column Multi-Grid prototype is tested [25] at the CNCS instrument. The detector columns consist of 2×48 grids, with 1 mm Gd_2O_3 shielding on the rear end of the grids, and a 2 mm thick MirroBor [36] rubber layer with 80 mass % natural B_4C content is also inserted between the columns to reduce cross-scattering.

The columns are placed in an aluminium vessel, as shown in Figure 6 and Figure 7, and the whole detector volume is filled with *counting gas*: Ar/CO_2 (80/20 by volume) at nominal room temperature and pressure. The Geant4 model of the detector was built with the same parameters.

In this model some of the instrument components are also present. The measurement chamber is filled with *tank gas*: Ar/CO_2 (98/2 by volume) at nominal room temperature and pressure. Tank gas is the gas in the cylindrical chamber on the flight path between the sample and the detector.

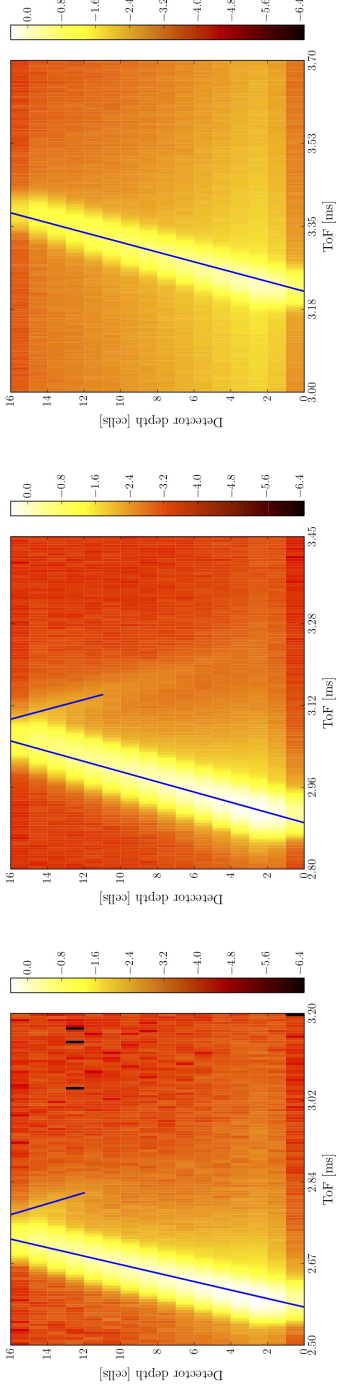
A simplified model of the sample environment is also implemented. It consists of a double-wall aluminium cylinder with radii of 10 and 12 cm and a 2 mm wall-thickness, representing the cryostat, and a 0.5 mm thick aluminium window with 74 cm radius (see Figure 8), representing the barrier between air and tank gas. In addition a 2° collimator is involved, placed between the cryostat and the aluminium window. The collimator is built of 136 pieces of 1 m high and 10 cm long stainless steel blades with $2 \times 10 \mu\text{m}$ Gd_2O_3 painting.

A significant effort has been made to understand and reduce the background in the Multi-Grid and other solid boron converter based detectors. As a part of this, the α -, γ - and fast neutron background components have been studied and reduced, as described in [34], [37] and [38], respectively. These background components are also omitted from the simulation, as the remnant background is negligible in comparison with the implemented instrument-related background sources [25].

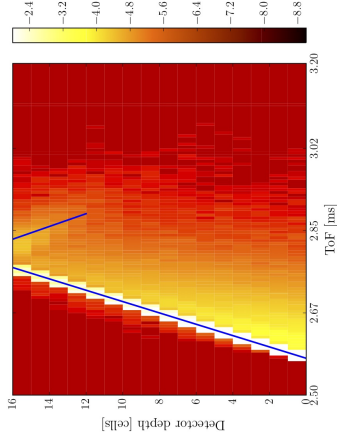
A series of tests are performed and published with this measurement setup, and the high statistics results with a vanadium sample [25] at 1.0, 3.678 and

3.807 meV (i.e. 9.04, 4.72 and 4.64 Å, respectively) are selected for simulating. In order to identify the scattered background components, the simulations are repeated with multiple geometry configurations, e.g. with and without sample environment or detector vessel, as well as with multiple neutron generators, e.g. a targeted beam irradiating the entire detector surface or a 4π -source, all with mono-energetic and Gaussian initial neutron energy distributions. The σ of the Gaussian distribution is chosen as 0.006 meV for the 1.0 and 0.030 meV for the 3.678 and 3.807 meV incident neutron energies, respectively, to fit the measured data, considering the known 1 % resolution of the CNCS instrument.

The complete model of detector & sample environment was checked with the simulation of the directly measured ToF and flight distance data.

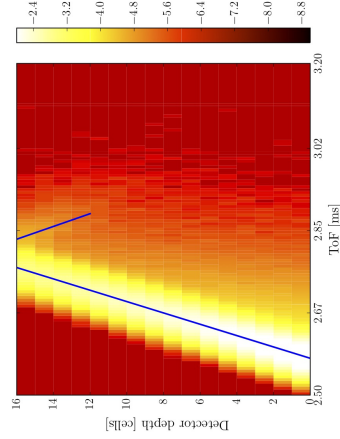


(a) Measured ToF at 4.1 Å.



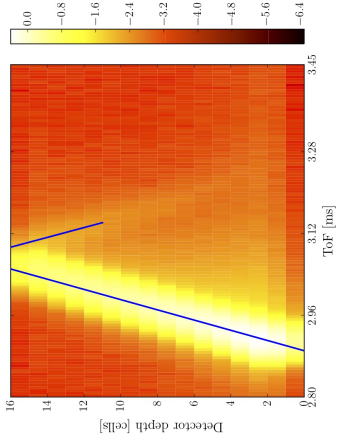
(d) Simulated ToF at 4.1 Å.

E_{ini} : mono-energetic

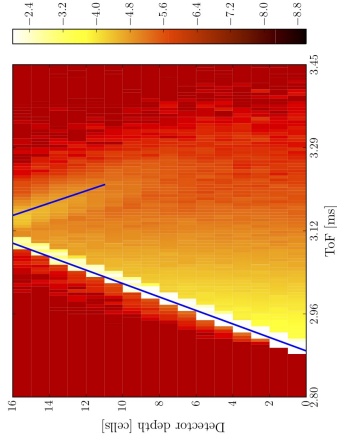


(g) Simulated ToF at 4.1 Å.

E_{ini} : Gaussian

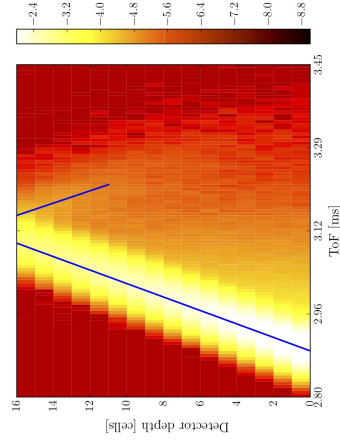


(b) Measured ToF at 4.6 Å.



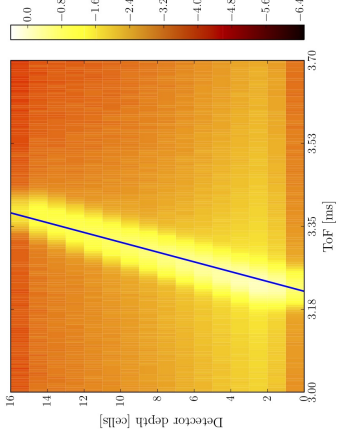
(e) Simulated ToF at 4.6 Å.

E_{ini} : mono-energetic

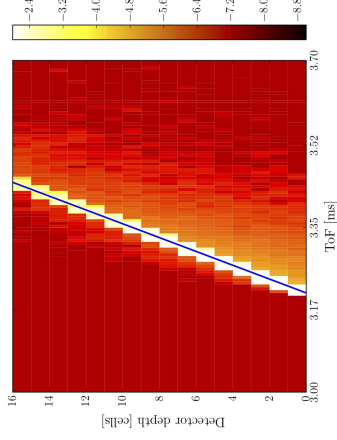


(h) Simulated ToF at 4.6 Å.

E_{ini} : Gaussian

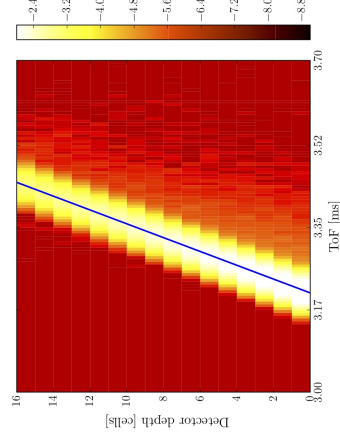


(c) Measured ToF at 5.1 Å.



(f) Simulated ToF at 5.1 Å.

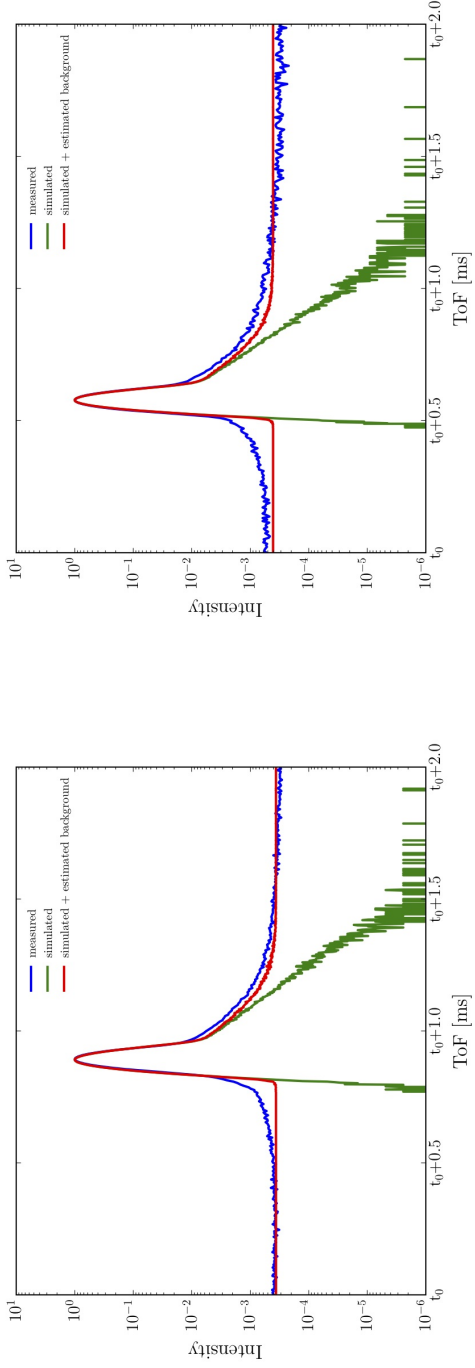
E_{ini} : mono-energetic



(i) Simulated ToF at 5.1 Å.

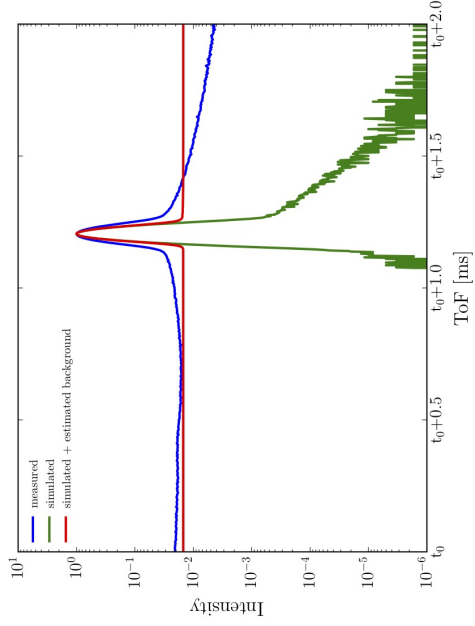
E_{ini} : Gaussian

Figure 4: Time-of-Flight spectra as a function of the detection depth. Results of measurement at the IN6 experiment (Figures 4a – 4c, measured data taken from [24]) and Geant4 simulation with mono-energetic (Figures 4d – 4f) and Gaussian (Figures 4g – 4i) initial energy distributions. Time-of-Flight measured from sample position. (The 3 black lines in Figure 4a are given by pixels with 0 counts due to low statistics.



(a) Simulated ToF at 4.6 Å.

(b) Simulated ToF at 4.1 Å.



(c) Simulated ToF at 5.1 Å.

Figure 5: Comparison of measured and simulated ToF spectra with and without α -background correction at 4.1 Å (5b), 4.6 Å (5a) and 5.1 Å (5c) in relative time-scale. Intensity of Time-of-Flight spectra is given as number of counts normalised to maximum. Measured data is taken from [24]. t_0 relates to the incidence of the neutron pulse on the sample position.

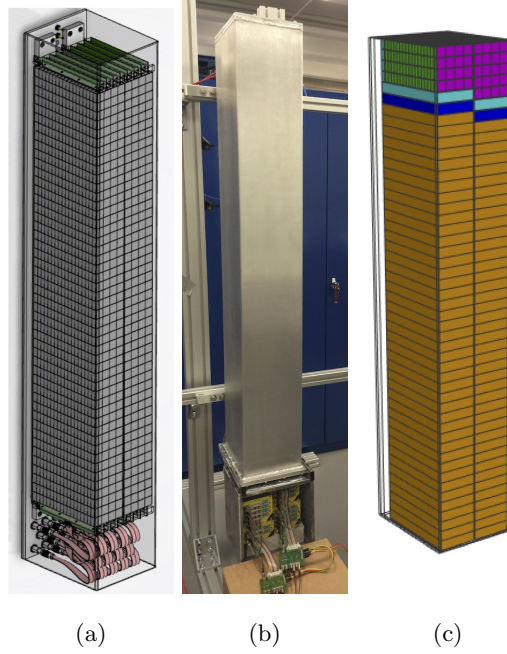


Figure 6: The CNCS demonstrator: technical drawing in CATIA V6 [39] (6a, source of plot: [25]), built prototype (6b, source of plot: [25]) and Geant4 model (6c).

4.1. Simulation results of primary measured data for CNCS demonstrator detector

The directly measured quantities, the ToF and the flight distance are simulated for checking the implemented detector and instrument setup of all the afore mentioned components.

The measured and simulated ToF and flight distance spectra at 3.678 and 3.807 meV incident neutron energies, below and above the aluminium Bragg-edge, are compared in Figures 9 and 10.

As shown in Figures 9a and 9b, a series of peaks appear in both measured and simulated flight distance spectra, relating to the geometrical cell structure of the grids. The resolution of the detector is affected by this cell structure, therefore these peaks are related to the rows of cells in the detector. The peaks are visible in the first 10–15 cm of the detector, where the majority of the

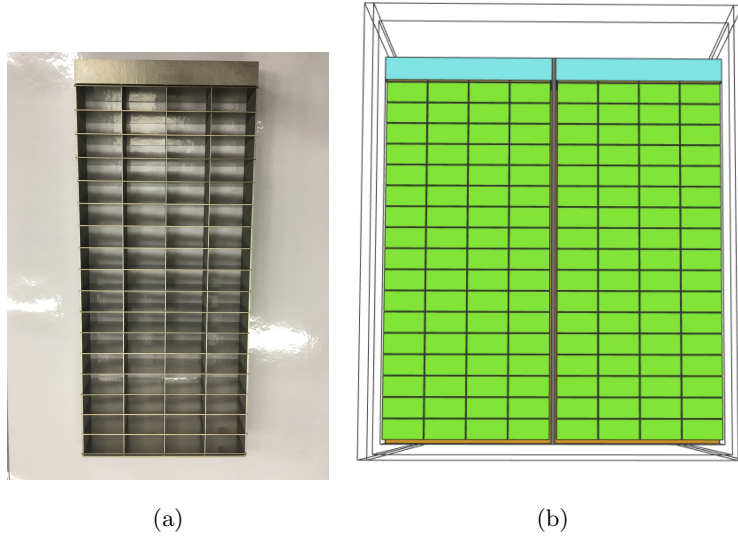


Figure 7: Layout of the CNCS demonstrator: single grid (7a) and Geant4 model (7b).

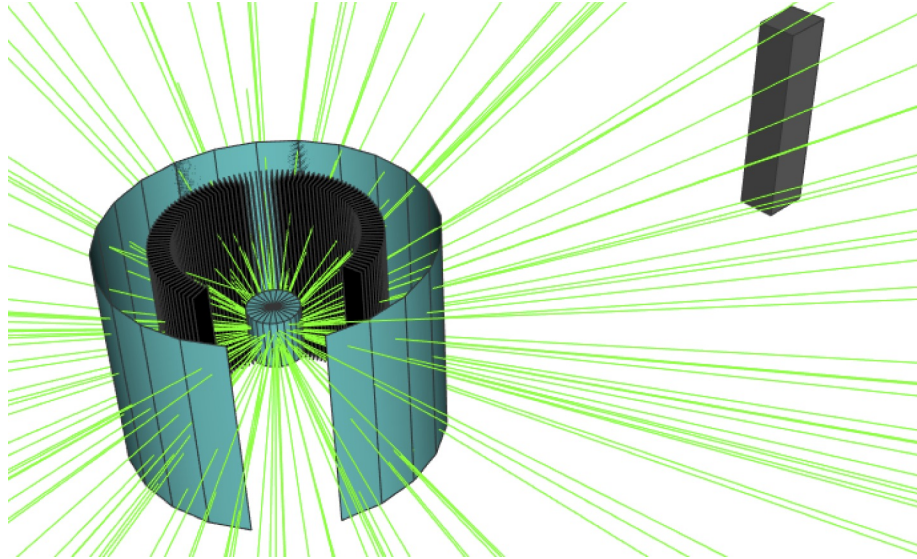
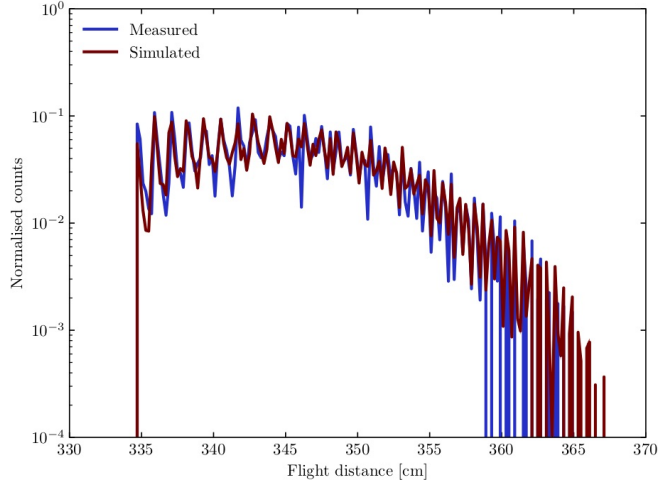


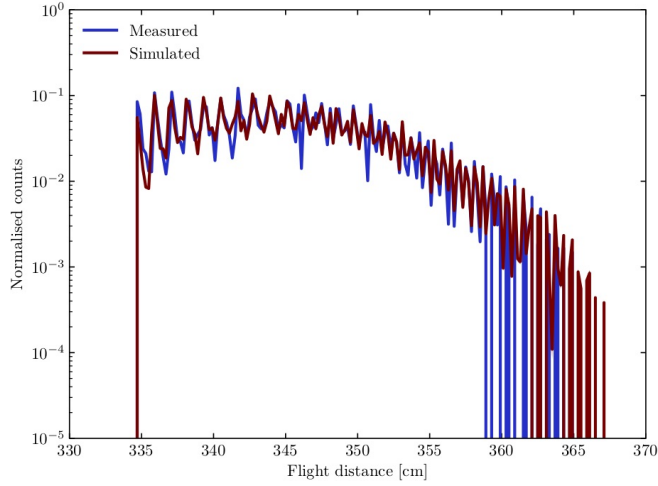
Figure 8: Geometry view of CNCS Geant4 model with sample environment, 4π -source and detector module.

neutrons are detected, therefore the statistics are the highest. The falling tail of the spectra is determined by the neutrons detected in the rear cells of the

detector, and by the scattered neutrons, having a longer flight distance. There is a difference in the cutoff of the two spectra, since the last row is not read out in the measurement, contrary to the simulation.



(a) Flight distance at 3.678 meV.



(b) Flight distance at 3.807 meV.

Figure 9: Measured and simulated flight distance spectra at 3.678 (9a) and 3.807 meV (9b) incident neutron energies, normalised to area.

Both the overlaying peaks and the characteristics of the falling tails of the measured and simulated spectra are in good agreement at both energies below and above the aluminium Bragg-edge.

The measured and simulated ToF spectra are compared in Figure 10. The simulated ToF is measured from the sample position, while the experimental data are given relatively to the 16667 μs period of the SNS pulse.

An arbitrary shift is applied on the measured spectra to overlay them with the simulated ones. This way the measured and simulated ToF peaks are fit at both energies; the shape and the width of the peaks give good agreement.

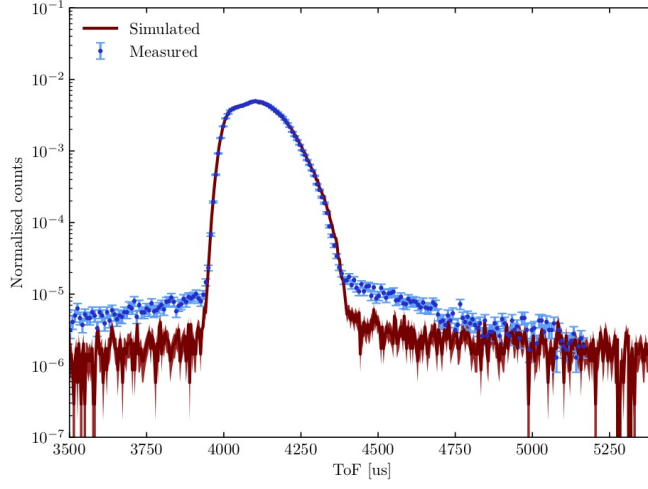
In both spectra the measured and simulated backgrounds also reasonably agree with the presence of some discrepancies between them. The source of these discrepancies is that not all instrument related effects are included in the simulation. For example instrument background radiation, initial ToF distribution of neutrons, and some of the sample environment components are omitted, since the aim of the current study focuses on understanding detector effects. However, the level of agreement of the measured and simulated backgrounds are acceptable, considering the diversity of backgrounds of the existing chopper spectrometers.

In essence, the measured and simulated ToF of elastic peaks agree well.

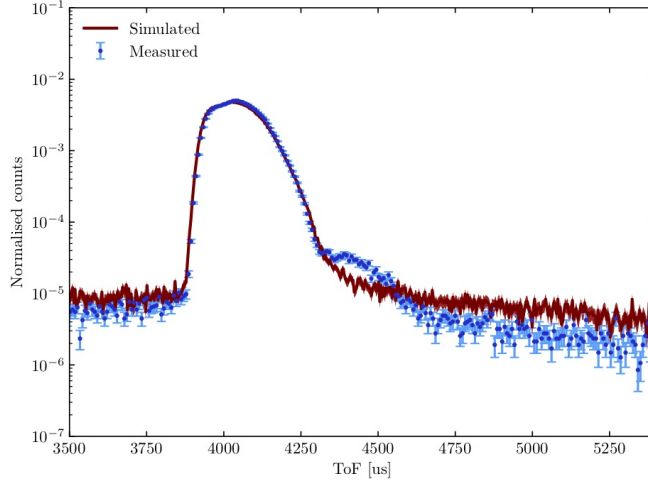
Therefore, the now tested CNCS irradiation setup can be used for performing detailed scattered neutron background study.

4.2. Energy transfer and background differentiation from measurement and simulation

Measured and simulated energy transfer spectra are compared as part of the validation process of the implemented Multi-Grid detector model. Simulations are also performed with different geometries, with the additional aim of identifying and distinguishing the sources of neutron scattering. The energy transfer is defined as $E_{trf} = E_{initial} - E_{final}$, therefore the elastic peak appears centred around 0 meV, while the negative side represents the neutrons detected with energy gain and the positive side represents the neutrons with energy loss



(a) ToF at 3.678 meV.



(b) ToF at 3.807 meV.

Figure 10: Measured and simulated Time-of-Flight spectra at 3.678 (10a) and 3.807 meV (10b) incident neutron energies, normalised to area.

in comparison with the initial energy. For this study the detector background is defined as all neutron events in the energy transfer spectrum outside of the elastic peak. Since the peaks are sharp and well-identifiable, the peak borders

are estimated visually. The background is always given normalised to the peak:

$$\text{background fraction} = \frac{\text{Total counts} - \text{Counts in peak}}{\text{Counts in peak}}. \quad (1)$$

The simulations are performed in the 1.0–8.0 meV incident neutron energy range. The measured and simulated energy transfer spectra at 1.0, 3.678 and 3.897 meV incident neutron energy, below and above the aluminium Bragg edge are presented in Figures 11a, 12a and 13a respectively. Simulations are repeated adding one-by-one the geometrical and instrumental components (see Section 4) to the simulation. The spectra are compared in Figures 11b, 12b and 13b, while the obtained scattered neutron background data are given in Table 2. “Bare detector grids” means two columns of grids, without the aluminium vessel.

In the energy transfer spectrum of the bare grids the elastic peak is mono-energetic at 0 meV and an asymmetric scattered neutron background also appears. The source of the background on the negative side is the neutrons that gained energy via inelastic scattering. The major source of higher and broader background on the positive side is the contribution of the elastically scattered neutrons. Since the flight distance is calculated from the detection coordinates, assuming the shortest path between the detection point and the sample, but the ToF measured represents the entire neutron path, in the case of elastic scattering a longer ToF is combined with a shorter flight distance, resulting to the registration of an effectively slower neutron. These neutrons have an apparent energy loss, and cause the asymmetrical, high intensity background. In Figure 13b a fine structure of peaks also appears near the elastic peak on the positive side: this peak relates to the grid structure, the coherent scattering between the aluminium blades. Therefore this effect appears only above the aluminium Bragg-edge.

A similar spectrum is obtained with the complete detector model inside the vessel. The scattered neutron background increases on both sides with respect to the one of the bare grids.

The effect of a Gaussian initial neutron energy distribution appears in Fig-

ures 11b, 12b and 13b; the initial energy distribution defines the shape of the elastic peak, while its impact on the background is negligible. The realistic Gaussian distribution only affects the background by the increased peak width. It is also apparent that the coherent scattering effects of the blades are hidden in the case of realistic incident neutron energy distributions.

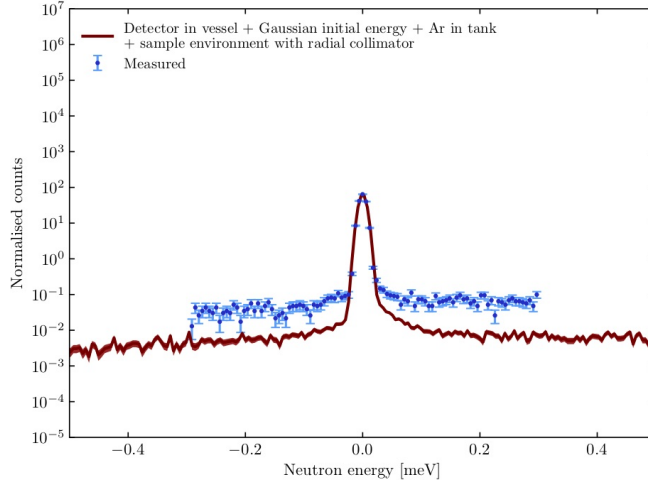
Including the tank gas and components of the sample environment, a continuous, flat scattered neutron background appears in the spectra. In all cases, the asymmetric detector background has a comparable shape, appearing as a shoulder on the side of the elastic peak. While at 1.0 meV (Figure 11b) and 3.678 meV (Figure 12b) the background is coming from the tank gas and the sample environment are comparable, at 3.807 meV (Figure 13b) the aluminium sample environment becomes the dominant source of background, significantly increasing the background. This background is slightly reduced by collimator, eliminating the scattered fraction of the cryostat and the backwall of the aluminium window. However, the sample environment remains the main background source above the Bragg-edge even in the presence of the collimator.

The measured data are compared with the most realistic case of the simulation, including all the afore described geometrical and instrumental components as in the case of the ToF and flight distance comparisons (see Section 4.1).

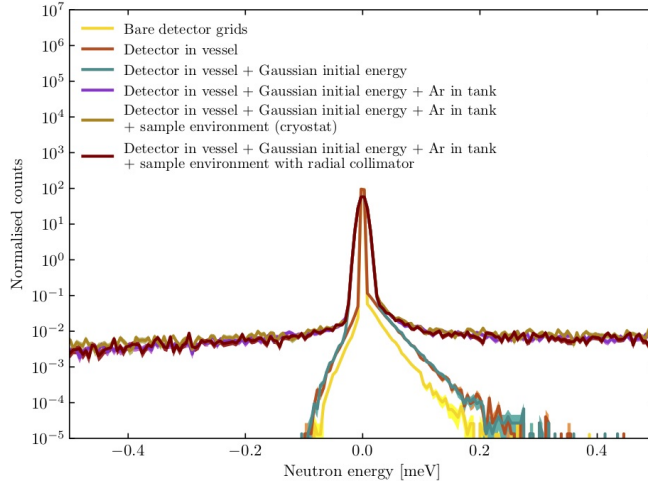
As it is shown in Figures 11a, 12a and 13a, the energy transfer spectra are reproduced by the simulation in all cases. In the case of 1.0 and 3.678 meV incident neutrons, below the aluminium Bragg-edge, the simulated background underestimates the measured one on both sides of the elastic peak. The discrepancy is about 80%. In the case of 3.807 meV incident neutrons, above the aluminium Bragg-edge, the simulated background slightly overestimates the measured one. The discrepancy is about 20% on the negative and 5% on the positive side of the elastic peak. The discrepancies in the background are attributed to the same reasons as for the primary quantities (see Section 4.1). It also has to be mentioned that the two bumps at 0.25 and 0.5 meV only appear in the measured energy transfer. This effect is related to the instrument, as it also appears in the response of local ^3He -tubes. Its independence from the presence of the

Multi-Grid detector is satisfactorily verified elsewhere.

In essence the measured and simulated elastic peaks agree well and the backgrounds reasonably agree at all energies.

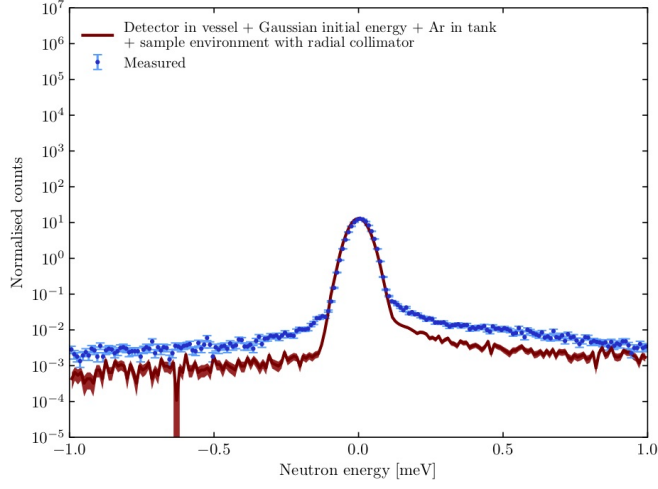


(a) Energy transfer at 1.0 meV.

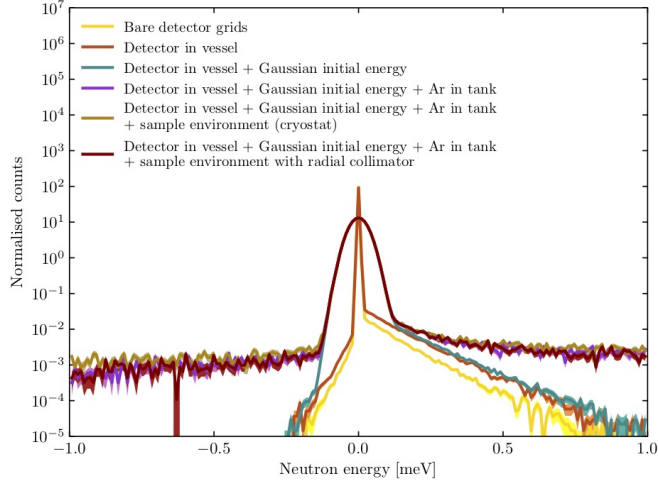


(b) Energy transfer at 1.0 meV.

Figure 11: Measured and simulated energy transfer at 1.0 meV incident neutron energy (11a) and comparison of the effect of different geometrical and instrumental parameters on energy transfer (11b). Energy transfer spectra are normalised to area.



(a) Energy transfer at 3.678 meV.



(b) Energy transfer at 3.678 meV.

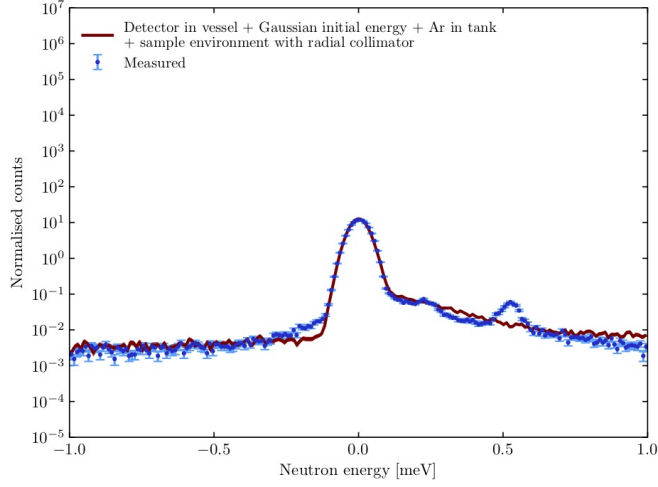
Figure 12: Measured and simulated energy transfer at 3.678 meV incident neutron energy (12a) and comparison of the effect of different geometrical and instrumental parameters on energy transfer (12b). Energy transfer spectra are normalised to area.

Table 2: Simulated scattered neutron background ratio, normalised to elastic peak area (See Equation 1). The peak is defined in two ways: manually fitted peak width, and fix $\Delta 0.052$ meV and $\Delta 0.24$ meV peak width, equal to peak width of results with $E_{ini, Gaussian}$ for 1 meV and 3.678 and 3.807 meV, respectively.

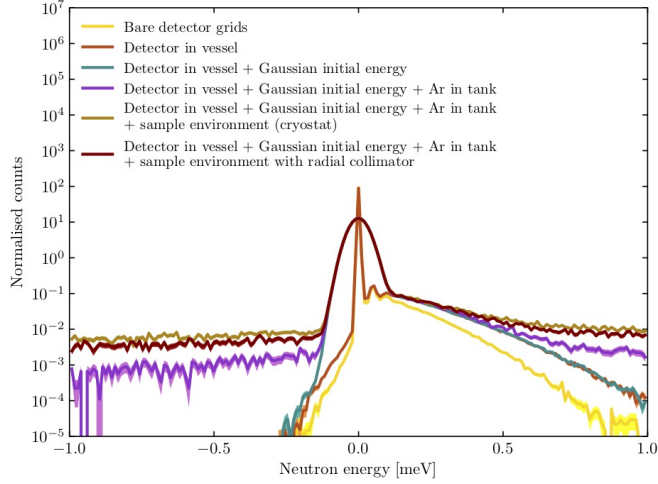
Model components	1.0 meV			3.678 meV			3.807 meV		
	Adaptive peak width	Fix ± 0.026 meV width	Adaptive peak width	Adaptive peak width	Fix ± 0.12 meV width	Adaptive peak width	Adaptive peak width	Fix ± 0.12 meV width	Adaptive peak width
	Background ratio [%]	Background ratio [%]	Background ratio [%]	Background ratio [%]	Background ratio [%]	Background ratio [%]	Background ratio [%]	Background ratio [%]	Background ratio [%]
Bare grids	0.18	0.04	0.23	0.06	1.80	0.82			
Detector in vessel	0.39	0.12	0.42	0.13	2.81	1.60			
Detector in vessel + Gaussian E_{ini}	0.14	0.12	0.16	0.16	1.70	1.57			
Detector in vessel + Gaussian E_{ini}	1.31	1.32	1.10	1.09	2.64	2.57			
+ Ar in tank									
Detector in vessel + Gaussian E_{ini}	1.72	1.71	1.42	1.42	6.90	6.62			
+ Ar in tank + sample environment									
Detector in vessel + Gaussian E_{ini}	1.30	1.26	1.08	1.07	5.11	4.88			
+ Ar in tank + sample environment with collimator									

Table 3: Simulated scattered neutron background ratio, normalised to elastic peak area (See Equation 1). The peak was defined with manually fitted peak width.

Vessel window	Grid entry	Vessel side	Vessel end	1.0 meV		3.678 meV		3.807 meV		8.0 meV	
				Background ratio [%]	Background ratio [%]	Background ratio [%]	Background ratio [%]	Background ratio [%]	Background ratio [%]	Background ratio [%]	Background ratio [%]
0 mm	0.5 mm	0 mm	0 mm	0.18	0.23	1.80	2.32				
0 mm	0.5 mm	3 mm	0 mm	0.30	0.33	2.63	3.20				
0 mm	2 mm	3 mm	0 mm	0.33	0.36	2.70	3.47				
3 mm	2 mm	3 mm	0 mm	0.39	0.41	2.79	3.84				
20 mm	2 mm	3 mm	0 mm	0.73	0.68	3.58	5.91				
3 mm	2 mm	3 mm	10 mm	0.39	0.41	2.81	3.86				



(a) Energy transfer at 3.807 meV.



(b) Energy transfer at 3.807 meV.

Figure 13: Measured and simulated energy transfer at 3.807 meV incident neutron energy (13a) and comparison of the effect of different geometrical and instrumental parameters on energy transfer (13b). Energy transfer spectra are normalised to area.

4.3. Optimisation of the detector vessel window

A study is performed with the CNCS demonstrator model on the effect of the aluminium window thickness and the vessel components. The window

thickness is defined as the sum of the vessel window and the entry grid thickness. The 0.5 mm grid entry thickness relates to the B₄C-coated blade, while bigger thicknesses indicate the presence of an additional entry blade. The effects of the other parts of the vessel, the side and the rear end are also considered. These components either appear with their realistic dimensions or are removed. Combination of thicknesses are tested and compared in the energy range of 1.0–8.0 meV in Figure 14. The set of simulated setups and the obtained backgrounds are presented in Table 3. The simulations are performed with mono-energetic incident neutrons irradiating the entire detector volume. Sample environment and tank gas are not present.

Comparing the results in the whole energy range it is shown that except for the 22 mm total window thickness, which is unrealistically thick, the difference in the background is negligible. However, the presence of the side wall causes a significant increase in the background on the positive side of the spectrum. Therefore, a realistically chosen window thickness practically does not change the scattered neutron background, but the application of shielding on the inner wall of the vessel might be considered.

5. Conclusions

This is the first time sources of thermal neutron scattering background are modelled in a detailed simulation of detector response.

A detailed, realistic and flexible Geant4 model of the Multi-Grid detector is built within the ESS Detector Group Simulation Framework. The model is validated against measured data from the demonstrators tested at the IN6 at ILL and the CNCS at SNS. Measured ToF data are reproduced for the IN6 experiment both qualitatively (ToF - detection depth spectra) and quantitatively (ToF spectra). The validated model is adopted for a more extensive set of measurements using a Multi-Grid detector at CNCS, including a more complete setup description. The model is verified with the comparison of measured and simulated ToF and flight distance data at 3.678 and 3.807 meV (below and

above the aluminium Bragg-edge).

A study is performed with the CNCS model to distinguish the sources of scattered neutron background. The elastic peak and the scattered neutron background in the energy transfer are now well-described and well-reproduced with the model, implying the predictive power of the simulation.

The simulation reveals that the neutron scattering in the detector geometry is minor in comparison with the effect of the scattering on instrument components: the tank gas and the sample environment; these are the major sources of the measured continuous flat background. The sample environment should also be considered in the recently built instruments, operating with vacuum tank. The effect of the detector window thickness is also studied in the range of 0.5 – 22 mm. It is shown that there is no significant change in the scattered neutron background for reasonable window thicknesses. The side of the vessel turns out to be a higher source of scattered neutron background, that should be taken into account in the further designs.

The availability of such a simulation allows to build neutron scattering instruments with optimised Signal-to-Background ratio by design.

Acknowledgements

This work has been supported by the In-Kind collaboration between ESS ERIC and the Hungarian Academy of Sciences, Centre for Energy Research (MTA EK). Richard Hall-Wilton, Anton Khaplanov and Thomas Kittelmann would like to acknowledge support from the EU Horizon2020 Brightness Grant [grant number 676548]. The authors would like to acknowledge the ILL and the SNS for the measured data. A portion of this research used resources at the Spallation Neutron Source, a DOE Office of Science User Facility operated by the Oak Ridge National Laboratory. CNCS data was measured at SNS under ID IPTS-17219. Computing resources provided by DMSC Computing Centre (<https://europeanspallationsource.se/data-management-software/computing-centre>).

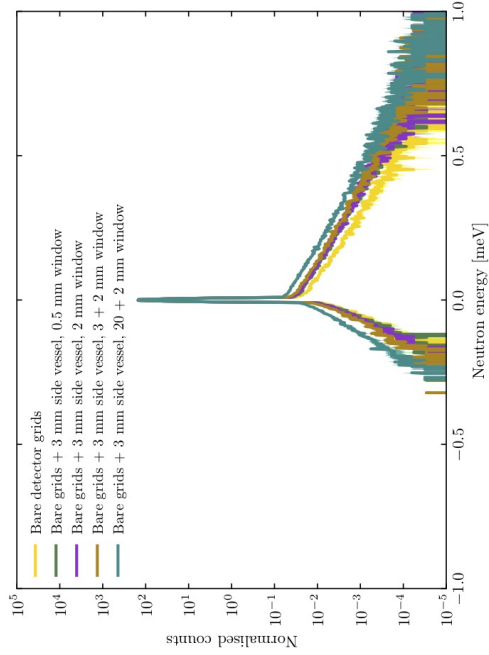
References

- [1] B. T. M. Willis, C. J. Carlile, Neutron Spectroscopy, in: B. T. M. Willis, C. J. Carlile (Eds.), *Experimental Neutron Scattering*, Oxford University Press, Oxford, 2009, Ch. 14-16, pp. 249–309.
- [2] J. Ollivier, H. Mutka, L. Didier, The new cold neutron time-of-flight spectrometer in5, *Neutron News* 21 (2) (2010) 22–25.
- [3] G. E. Granroth, et al., SEQUOIA: A fine resolution chopper spectrometer at the SNS, *Physica B: Condensed Matter* 385-386, Part 2 (2006) pp. 1104–1106. doi:10.1016/j.physb.2006.05.379.
- [4] G. Ehlers, et al., The New Cold Neutron Chopper Spectrometer at the Spallation Neutron Source: Design and Performance, *Review of Scientific Instruments* 82 (085108). doi:10.1063/1.3626935.
- [5] G. Ehlers, et al., The New Cold Neutron Chopper Spectrometer at the Spallation Neutron Source - a review of the first 8 years of operation, *Review of Scientific Instruments* 87 (093902). doi:10.1063/1.4962024.
- [6] R. Kajimoto, et al., The Fermi Chopper Spectrometer 4SEASONS at J-PARC, *J. Phys. Soc. Jpn.* 80 (SB025). doi:10.1143/JPSJS.80SB.SB025.
- [7] K. Nakajima, et al., AMATERAS: A Cold-Neutron Disk Chopper Spectrometer, *J. Phys. Soc. Jpn.* 80 (SB028). doi:10.1143/JPSJS.80SB.SB028.
- [8] R. I. Bewley, et al., LET, a Cold Neutron Multi-Disk Chopper Spectrometer at ISIS, *Nuclear Instruments and Methods in Physics Research Vol. 637*, Issue 1 (2011) pp. 128–134. doi:10.1016/j.nima.2011.01.173.
- [9] D. Shea, D. Morgan, The Helium-3 shortage: supply, demand, and options for congress, Tech. Rep. R41419, Congressional Research Service (December 2010).
- [10] K. Zeitelhack, ICND, *Neutron News* 23 (4) (2012) 10–13.

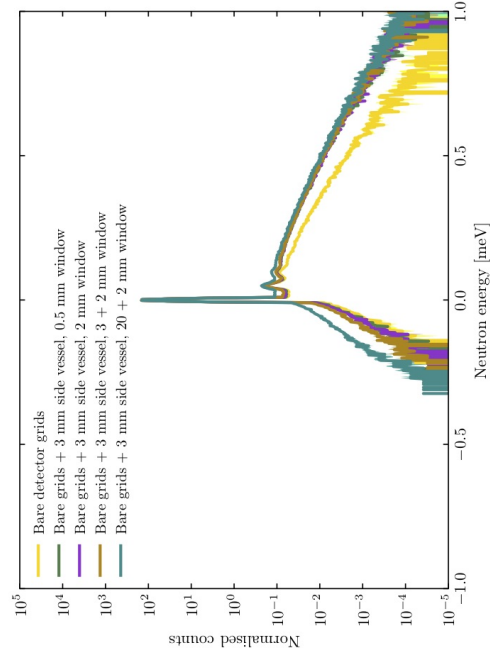
- [11] K. Andersen, et al., 10B multi-grid proportional gas counters for large area thermal neutron detectors, Nucl. Instr. and Meth. A 720 (2013) 116–121.
- [12] A.Khaplanov, 10b multi-grid proportional gas counters for large area thermal neutron detectors, Neutron News 23 (2012) 25.
- [13] European Spallation Source ESS ERIC.
URL <http://europeanspallationsource.se/>
- [14] P. P. Deen, et al., A design study of VOR: a Versatile Optimal Resolution chopper spectrometer for the ESS, EPJ Web of Conferences 83 (03002).
doi:10.1051/epjconf/20158303002.
- [15] T. Brückel, J. Voigt, N. Violini, A. Orecchini, A. Paciaroni, F. Sacchetti, M. Zanatt, ESS Instrument Construction Proposal T-REX: A Time-of-flight Reciprocal space Explorer.
- [16] W. Lohstroh, W. Petry, J. Neuhaus, L. Silvi, C. Alba-Simionesco, J.-M. Zanotti, S. Longeville, ESS Instrument Construction Proposal C-SPEC - Cold chopper spectrometer.
- [17] B. Guerard, J.-C. Buffet, no. US 2011215251, (Laue Max Inst, France), 2010.
- [18] Institute Laue-Langevin.
URL <http://www.ill.eu>
- [19] The Cluster of Research Infrastructures for Synergies in Physics.
URL www.crisp-fp7.eu
- [20] BrightnESS.
URL <https://brightness.esss.se/>
- [21] C. Höglund, B4C thin films for neutron detection, J. Appl. Phys. 111 (2012) (104908).

- [22] C. Höglund, et al., Stability of $^{10}\text{B}_4\text{C}$ thin films under neutron radiation, *Radiation Physics and Chemistry* 113 (2015) 14–19.
- [23] S. Schmidt, et al., Low-temperature growth of boron carbide coatings by direct current magnetron sputtering and high-power impulse magnetron sputtering, *Journal of Materials Science* 51. doi:10.1007/s10853-016-0262-4.
- [24] A. Khaplanov, et al., In-beam test of the Boron-10 Multi-Grid neutron detector at the IN6 time-of-flight spectrometer at the ILL, *J. Phys.: Conf. Ser.* 528 (2014) (012040).
- [25] A. Khaplanov, et al., Multi-Grid Detector for Neutron Spectroscopy: Results Obtained on Time-of-Flight Spectrometer CNCS, *JINST* 12 (2017) P04030.
- [26] S. Agostinelli, et al., Geant4: A simulation toolkit, *Nucl. Instr. and Meth. A* 506 (2003) 250–303.
- [27] J. Allison, et al., Geant4 developments and applications, *IEEE Trans.Nucl. Sci.* vol. 53 (no. 1) (2006) pp. 270–278. doi:10.1109/TNS.2006.869826.
- [28] J. Allison, et al., Recent developments in geant4, *Nucl. Instrum. Methods Phys. Res. Section A Accel. Spectrometers Detect. Assoc. Equip.* vol. 835 (2016) pp. 186–225. doi:10.1016/j.nima.2016.06.125.
- [29] T. Kittelmann., et al., Geant4 based simulations for novel neutron detector development, *J. Phys.: Conf. Ser Vol.* 513. doi:doi:10.1088/1742-6596/513/2/022017.
- [30] T. Kittelmann, M. Boin, Polycrystalline neutron scattering for Geant4: NXSG4, *Comput. Phys. Commun.* 189 (2015) pp. 114–118. doi:doi:10.1016/j.cpc.2014.11.009.
- [31] T. Kittelmann, K. Kanaki, E. Klinkby, X. X. Cai, C. P. Cooper-Jensen, R. Hall-Wilton, Using backscattering to enhance efficiency in neutron de-

- tectors, IEEE Transactions on Nuclear Science 64 (6) (2017) pp. 1562–1573.
doi:10.1109/TNS.2017.2695404.
- [32] S. T. Thornton, A. Rex, Modern Physics for Scientists and Engineer, Saunders College Publishing, 1993.
- [33] E. A. Owen, E. L. Yates, Precision measurements of crystal parameters, Philosophical Magazine 15 (1933) pp. 472–488.
- [34] J. Birch, et al., Investigation of background in large-area neutron detectors due to alpha emission from impurities in aluminium, Journal of Instrumentation 10 (2015) P10019. doi:10.1088/1748-0221/10/10/P10019.
- [35] J. Peters, J. D. M. Champion, G. Zsigmond, H. N. Bordallo, F. Mezei, Using Fermi choppers to shape the neutron pulse, NIM A 557 (2) (2006) pp. 580–584. doi:10.1016/j.nima.2005.11.111.
- [36] Mirrotron Radiation Shielding.
URL <https://mirrotron.com/en/products/radiation-shielding>
- [37] A. Khaplanov, et al., Investigation of gamma-ray sensitivity of neutron detectors based on thin converter films, JINST 8 (2013) (P10025). doi:10.1088/1748-0221/8/10/P10025.
- [38] G. Mauri, et al., Fast neutron sensitivity of neutron detectors based on boron-10 converter layers, Journal of Instrumentation 13 (2018) P03004. doi:10.1088/1748-0221/13/03/P03004.
- [39] CATIA6.
URL <https://www.3ds.com/products-services/catia/products/v6/>

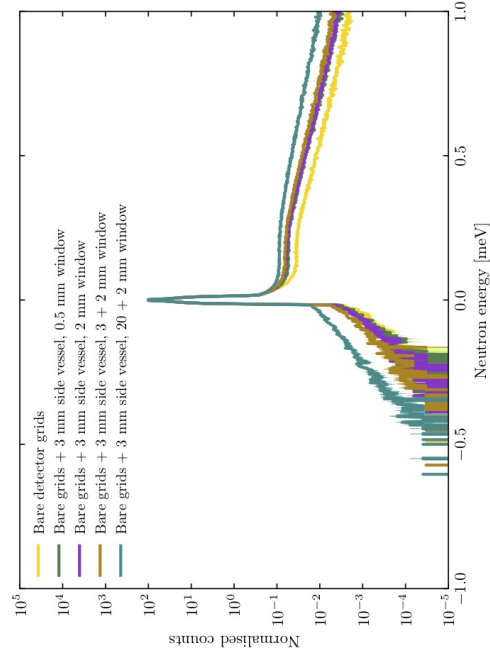


(a) Energy transfer at 1.0 meV.



(c) Energy transfer at 3.807 meV.

(b) Energy transfer at 3.678 meV.



(d) Energy transfer at 8.0 meV.

Figure 14: Simulated energy transfer, with the presence of different window thicknesses and vessel components. Results are normalised to area.